Atmospheric
Chemistry
and Physics
Discussions

On the drivers of droplet variability in Alpine mixed-phase clouds

Paraskevi Georgakaki[1], Aikaterini Bougiatioti[2], Jörg Wieder[3], Claudia Mignani[4], Fabiola Ramelli[3], Zamin A. Kanji[3], Jan Henneberger[3], Maxime Hervo[5], Alexis Berne[6], Ulrike Lohmann[3] and Athanasios Nenes[1,7]

[1]Laboratory of Atmospheric Processes and their Impacts, School of Architecture, Civil & Environmental Engineering, École Polytechnique Fédérale de Lausanne, Lausanne, CH-1015, Switzerland
[2]Institute for Environmental Research & Sustainable Development, National Observatory of Athens, P. Penteli, GR-15236, Greece
[3]Department of Environmental Systems Science, Institute for Atmospheric and Climate Science, ETH Zurich, Zurich, CH-8092, Switzerland
[4]Department of Environmental Sciences, University of Basel, Basel, CH-4056, Switzerland
[5]Federal Office of Meteorology and Climatology, MeteoSwiss, Payerne, CH-1530, Switzerland
[6]Environmental Remote Sensing Laboratory, School of Architecture, Civil & Environmental Engineering, École Polytechnique Fédérale de Lausanne, Lausanne, CH-1015, Switzerland
[7]Center for Studies of Air Quality and Climate Change, Institute of Chemical Engineering Sciences, Foundation for Research and Technology Hellas, Patras, GR-26504, Greece

Correspondence to: Athanasios Nenes (athanasios.nenes@epfl.ch).

Abstract

Droplet formation provides a direct microphysical link between aerosols and clouds (liquid or mixed phase), and its adequate description poses a major challenge for any atmospheric model. Observations are critical for evaluating and constraining the process. Towards this, aerosol size distributions, cloud condensation nuclei, hygroscopicity and lidar-derived vertical velocities were observed in Alpine mixed-phase clouds during the Role of Aerosols and Clouds Enhanced by Topography on Snow (RACLETS) field campaign in the Davos, Switzerland region during February and March 2019. Data from the mountain-top site of Weissfluhjoch (WFJ) and the valley site of Davos Wolfgang are studied. These observations are coupled with a state-of-the art droplet activation parameterization to investigate the aerosol-cloud droplet link in mixed-phase clouds. The mean CCN-derived hygroscopicity parameter, κ, at WFJ ranges between 0.2-0.3, consistent with expectations for continental aerosol. κ tends to decrease with size, possibly from an enrichment in organic material associated with the vertical transport of fresh ultrafine particle emissions (likely from biomass burning) from the valley floor in Davos. The parameterization provides droplet number that agrees with observations to within ~25%. We also find that the susceptibility of droplet formation to aerosol concentration and vertical velocity variations can be appropriately described as a function of the standard deviation of the distribution of updraft velocities, σ_w, as the droplet number never exceeds a characteristic limit, termed "limiting droplet number", of ~150-550 cm^{-3}, which depends solely on σ_w. We also show that high aerosol levels in the valley, most likely from anthropogenic activities, increase

41   cloud droplet number, reduce cloud supersaturation (<0.1%) and shift the clouds to a state that

42   is less susceptible to aerosol and become very sensitive to vertical velocity variations. The

43   transition from aerosol to velocity-limited regime depends on the ratio of cloud droplet number

44   to the limiting droplet number, as droplet formation becomes velocity-limited when this ratio

45   exceeds 0.5. Under such conditions, droplet size tends to be minimal, reducing the likelihood

46   that large drops are present that promote glaciation through rime splintering and droplet

47   shattering. Identifying regimes where droplet number variability is dominated by dynamical –

48   rather than aerosol – changes is key for interpreting and constraining when and which types of

49   aerosol effects on clouds are active.

50

51   **1.   Introduction**

52   Orographic clouds, and the precipitation they generate, play a major role in Alpine weather and

53   climate (e.g., Roe, 2005; Grubisic and Billings, 2008; Saleeby et al., 2013; Vosper et al., 2013;

54   Lloyd et al., 2015). The formation and evolution of orographic clouds involves a rich set of

55   interactions at different spatial and temporal scales encompassing fluid dynamics, cloud

56   microphysics and orography (Roe, 2005; Rotunno and Houze, 2007). Atmospheric aerosol

57   particles modulate the microphysical characteristics of orographic clouds by serving as cloud

58   condensation nuclei (CCN) that form droplets, or ice nucleating particles (INPs) that form ice

59   crystals (e.g., Pruppacher and Klett, 1997; Muhlbauer and Lohmann, 2009; Zubler et al., 2011;

60   Saleeby et al., 2013).

61   Emissions of aerosol particles acting as CCN and INPs can affect the microphysical and

62   radiative properties of clouds with strong (but highly uncertain) effects on local and regional

63   climate (IPCC, 2013; Seinfeld et al., 2016). Aerosol interactions with orographic clouds are

64   subject to even larger uncertainties, owing in part to the complex flows generated by the

65   interaction of the large-scale flow with the mesoscale orographic lifting and condensation, and

66   complex anisotropic turbulent air motions that arise (Roe, 2005; Smith, 2006; Rotunno and

67   Houze, 2007). Most importantly, orographic clouds are often mixed-phase clouds (MPCs),

68   which are characterized by the simultaneous presence of supercooled liquid water droplets and

69   ice crystals (Lloyd et al., 2015; Farrington et al., 2016; Lohmann et al., 2016; Henneberg et al.,

70   2017). MPCs remain one of the least understood cloud types, due to the multiple and highly

71   nonlinear cloud microphysical pathways that can affect their properties and evolution. MPCs

72   tend to glaciate (i.e., transition to pure ice clouds) over time because of the Bergeron-Findeisen

73   process, which is the rapid growth of ice crystals at the expense of the evaporating cloud

74   droplets, owing to the higher saturation vapor pressure of liquid water over ice (Bergeron,

75   1935; Findeisen, 1938). Aerosol concentrations may also alter the microphysical pathways

76   active in MPCs and ultimately drive their glaciation state. For instance, increase in CCN

77   concentrations leads to more numerous and smaller cloud droplets, reducing the riming

78   efficiency of ice crystals and therefore the hydrometeor crystal mass and the amount of

79   precipitation (Lohmann and Feichter, 2005; Lance et al., 2011; Lohmann, 2017). This

80   mechanism counters the glaciation indirect effect, where increases in INP concentrations

81   elevate ice crystal number concentration (ICNC) and promotes the conversion of liquid water

82   to ice - therefore the amount of ice-phase precipitation (Lohmann, 2002). Increases in CCN

83   can also decrease cloud droplet radius, and impede cloud glaciation, owing to reductions in

84   secondary ice production (SIP), which includes rime splintering, collisional break-up and

85   droplet shattering (Field et al., 2017; Sotiropoulou et al., 2020a, 2020b).

86   Cloud-scale updraft velocity (i.e., the part of the vertical velocity spectrum with positive

87   values) is the major driver of droplet formation, owing to the supersaturation generated from

88   adiabatic expansion and cooling (e.g., Nenes et al., 2001; Ghan et al., 2011). Despite its

89   importance, the simulation of updraft velocity by atmospheric models is rarely constrained by

90   observations, which can lead to large uncertainties in climate and numerical weather prediction

91   models (Sullivan et al., 2016, 2018). Reutter et al. (2009) pointed out that droplet formation in

92   clouds can be limited by the amount of CCN present (called the "aerosol-limited" regime), or

93   the vertical velocity that generates supersaturation in the cloudy updrafts (called the "velocity-

94   limited" regime). Over the complex Alpine terrain, vertical motions can be significantly shaped

95   by the effects of orography (Lohmann et al., 2016). Orographic MPCs have been frequently

96   observed in the Swiss Alps under high updraft velocity conditions, where supersaturation with

97   respect to liquid water is formed faster than it is depleted by diffusional and collisional ice

98   growth processes (Korolev and Isaac, 2003) leading to persistent MPCs (Lohmann et al., 2016).

99   Given the importance of droplet number for the radiative cloud properties and

100   microphysical evolution of Alpine MPCs, it is essential to understand the main aerosol and

101   dynamics properties that drive droplet formation. A limited number of studies exist that discuss

102   this very important topic, focusing though on liquid-phase clouds (Hammer et al., 2014, 2015;

103   Hoyle et al., 2016). Hoyle et al. (2016) demonstrated that 79% of the variance in droplet number

104   observed in warm tropospheric clouds formed over the high-altitude research station of

105   Jungfraujoch (3450 m a.s.l.) in the Swiss Alps can be explained by the potential CCN number

106   concentrations (i.e. aerosol particles with a dry diameter >80 nm). With box model simulations,

107   Hammer et al. (2015) investigated the influence of updraft velocity, particle concentration and

108 hygroscopicity on droplet formation in cloud updraft, and found that variations in vertical wind

109 velocity have the strongest influence on aerosol activation. The ability to predict droplet

110 number in MPCs, where the existence of ice crystals can deplete supersaturation or the low

111 temperatures may decrease CCN activity through the formation of glassy aerosol, has not been

112 assessed in a closure study to date.

113   Here we analyze observational data collected as part of the Role of Aerosols and Clouds

114 Enhanced by Topography on Snow (RACLETS) field campaign, which was held in the region

115 of Davos, Switzerland, during February and March 2019. This intensive field campaign aims

116 to address questions related to the modulators of orographic precipitation, the drivers of the

117 enhanced ice-crystal number concentrations observed in MPCs as well as the human-caused

118 pollution effects on cloud microphysical and optical properties. Through this study we focus

119 on a two-week period seeking to unravel the complex aerosol-droplet-updraft velocity

120 interactions that occur in the orographic MPCs. For this, we combine CCN number

121 concentrations with the particle size distributions to understand the variations in hygroscopicity

122 over time and for sites located in the valley and a close by mountain-top site. The in-situ

123 measurements are subsequently coupled with a state-of-the art droplet parameterization to

124 determine the potential droplet numbers and the corresponding maximum supersaturation

125 achieved in cloudy updrafts. The predicted droplet numbers are evaluated against direct

126 observations, and the degree to which droplet formation is velocity- or aerosol-limited is

127 determined for the whole timeseries.

128

2. Methods

130 2.1 Observational datasets

131 The analysis utilizes measurements collected during the RACLETS campaign, which took

132 place from 8 February to 28 March 2019 (https://www.envidat.ch/group/about/raclets-field-

133 campaign) (Mignani et al., 2020; Ramelli et al., 2020b, c; Lauber et al., 2020). This joint

134 research project offers a unique dataset of orographic clouds, precipitation and snow

135 measurements in an effort to shed light on some fundamental microphysical processes being

136 present in subsequent stages of the lifecycle of clouds (i.e. cloud formation, precipitation onset,

137 cloud dissipation). All measurements presented in this paper were performed at two distinct

138 observation stations near Davos, Switzerland (supplement Fig. S1). A measurement site is

139 located at Davos Wolfgang, which is the pass between Davos (1560 m a.s.l.) in the South and

140 Klosters (1200 m a.s.l.) in the North and is otherwise known as Wolfgang-Pass (WOP; 1630

141 m a.s.l., 46°50'08.076″N 9°51′12.939″E). Measurements were also conducted at the mountain-

142 top station Weissfluhjoch (WFJ; 2700 m a.s.l., 46°49'58.670″N 9°48′23.309″E), which is

143 located ‿1 km above the valley floor in Davos, in the eastern part of the Swiss Alps. The

144 current study primarily focuses on data collected during a two-week period of interest, which

145 spans from 24 February to 8 March 2019. During the RACLETS campaign, a defective sheath

146 air filter affected the CCN measurements collected at WFJ, thus inhibiting data usage from the

147 instrument for a large duration of the campaign. Therefore, we limit our analysis to the above-

148 mentioned period, when the CCN counter was fully operational. Besides, during the selected

149 period two distinct weather patterns were observed (fair weather conditions interrupted by a

150 precipitating period), allowing for a contrasting analysis of the observed scenarios. The

151 following description refers to the measurements that provided the basis for the present analysis

152 (see Table 1).

153

154 *2.1.1 Aerosol particle size distribution measurements*

155 Particle size distributions were continuously monitored at WOP and WFJ using commercially

156 available Scanning Mobility Particle Sizers (SMPS; Model 3938, TSI Inc., US). At both

157 stations, the systems consisted of a differential mobility analyzer (Model 3081, TSI Inc., US),

158 a soft X-ray neutralizer (Model 3088, TSI Inc., US) and a water-based condensation particle

159 counter (Model 3787 at WOP, Model 3788 at WFJ, TSI Inc. US). Running the particle counters

160 in low flow mode (0.6 Lmin^{-1}), using a sheath flow of 5.4 Lmin^{-1} and applying a total scanning

161 time of 2 minutes (scan time: 97 s, retrace time: 3 s, purge time: 10 s), particle size distributions

162 between 11.5 nm and 469.8 nm were monitored.

163

164 *2.1.2 CCN measurements*

165 A Droplet Measurement Technologies (DMT) single-column continuous-flow streamwise

166 thermal gradient chamber (CFSTGC; Roberts and Nenes, 2005) was used to carry out in-situ

167 measurements of CCN number concentrations for different supersaturations (*SS*). The

168 CFSTGC consists of a cylindrical flow tube with wetted walls, inside which *SS* is developed

169 by applying a linear streamwise temperature gradient between the column top and bottom.

170 Owing to the greater mass diffusivity of water vapor than the thermal diffusivity of air, a

171 constant and controlled *SS* is generated with a maximum at the centerline of the flow tube. The

172 *SS* is mainly dependent on the applied temperature gradient, flow rate and pressure (Roberts

173 and Nenes, 2005). An aerosol sample flow is introduced at the column centerline, and those

174 particles having a critical supersaturation lower than the instrument *SS* will activate to form

175 droplets and will afterward be counted and sized by an Optical Particle Counter (OPC) located

176 at the base of the CFSTGC column. The *SS* developed within the instrument responds linearly

177 to changes in pressure, since its operation relies on the difference between heat and mass

178 diffusivity. Calibration of the instrument, which determines the output supersaturation, was

179 performed by the manufacturer at ~800 mbar, while throughout the campaign the CFSTGC

180 was operating at a lower pressure ~735 mbar, therefore the *SS* reported by the instrument is

181 adjusted by a factor of $\frac{735}{800} = 0.92$, which takes into account the difference between the

182 ambient and the calibration pressure (Roberts and Nenes, 2005). CCN concentrations were

183 measured at a specific *SS* for approximately 10 minutes; the instrument was cycled between 6

184 discrete values ranging from 0.09% to 0.74% supersaturations, producing a full spectrum every

185 hour. Each 10-minute segment of the raw CCN data are filtered to discount periods of transient

186 operation (during supersaturation changes), and whenever the room temperature housing the

187 instrument changed sufficiently to induce a reset in column temperature (the instrument control

188 software always sets the column temperature to be at least 1.5 degrees above the room

189 temperature to exclude spurious supersaturation generation in the column inlet). The CFSTGC

190 was deployed on the mountain-top site of WFJ with the intention of relating the CCN

191 measurements directly to the size distribution and total aerosol concentration data measured by

192 the SMPS instrument at the same station.

193

194 *2.1.3 Cloud microphysical measurements*

195 In-situ observations of the cloud microphysical properties were obtained with the tethered

196 balloon system HoloBalloon (Ramelli et al., 2020a). The main component of the measurement

197 platform is the holographic cloud imager HOLIMO 3B, which uses digital in-line holography

198 to image an ensemble of cloud particles in the size range from 6 μm to 2 mm diameter in a

199 three-dimensional detection volume. Based on a set of two-dimensional images, information

200 about the particle position, size and shape can be obtained. The detected particles can be

201 classified as cloud droplets and ice crystals using supervised machine learning (Fugal et al.,

202 2009; Touloupas et al., 2020). The differentiation is possible for particles larger than 25 μm.

203 From the classification, the phase-resolved size distribution, concentration and content can be

204 derived (Henneberger et al., 2013; Ramelli et al., 2020a). HOLIMO has an open path

205 configuration (i.e. the detection volume lies between the two instrument towers) and thus is

206 also able to measure raindrops up to a size of ⌣2 mm. The HoloBalloon platform was flying at

207 WOP and provided vertical profiles of the cloud properties within the lowest 300 meters of the

208 boundary layer (BL). The current analysis utilizes the cloud droplet number concentration and

209 liquid water content (LWC) measurements. Note that the LWC is calculated based on the

210 measured number concentration and size distribution using a water density of 1000 kg m^{-3} and

211 is therefore dominated by large cloud particles.

212

213 **Table 1.** Overview of data sources from the RACLETS campaign used for this study. Along
214 with the observed parameters, the corresponding instrumentation, measurements range and
215 time resolutions are listed.

Measured parameter	Measurement site	Instrument	Measurement range	Time resolution
Aerosol number size distribution	WOP/ WFJ	Scanning Mobility Particle Sizer	11.5 – 469.8 nm	2 min
CCN number concentration	WFJ	Continuous flow streamwise thermal gradient CCN counter	SS = 0.09 – 0.74%	1 s
Cloud droplet number concentration and liquid water content	WOP	Holographic cloud imager HOLIMO	6 μm – 2 mm	10 – 20 s
Precipitation	WOP/ WFJ	Parsivel disdrometer/ MeteoSwiss weather station	0.2 mm – 25 mm	30 s
Horizontal wind speed and direction	WOP/ WFJ	MeteoSwiss weather station	–	10-min averages
Profiles of vertical wind speed	WOP	Wind Doppler Lidar	200 m – 8100 m AGL	up to 5 s

216

217 *2.1.4 Meteorological data*

218 During the measurement period, meteorological parameters (e.g., pressure, temperature,

219 precipitation, horizontal wind speed and direction) were continuously monitored by the

220 permanent MeteoSwiss observation station at WFJ. Additionally, a weather station was

221 installed on the OceaNet container (Griesche et al., 2019) deployed at WOP, which also hosted

222 several remote sensing instruments (e.g., Cloud radar, Raman Lidar, Microwave radiometer)

223 and a Particle Size Velocity (Parsivel) disdrometer (Parsivel2, OTT HydroMet GmbH,

224 Germany; Tokay et al., 2014) to measure precipitation. As there was no wind sensor included

225 in the weather station on the OceaNet container, we utilized the horizontal wind speed and

226 direction measurements from the nearby MeteoSwiss station in Davos, assuming that they

227 provide a good proxy for the wind regime in the valley. Vertical wind speed profiles were

228 obtained with a wind Doppler Lidar (WindCube 100S, manufactured by Leosphere) at WOP.

229 Throughout the campaign the wind lidar measured from 200 m to 8100 m above ground level

230 (AGL) with high temporal (up to 5 s) and vertical resolution (50 m). The wind lidar operated

231 following the Doppler Beam Switching (DBS) technique with an elevation of 75°. More

232 information about the remote sensing measurements can be found in Ramelli et al. (2020b).

233

234 **2.2 Aerosol hygroscopicity**

235 The aerosol hygroscopicity parameter, κ, encompasses the impact of particle chemical

236 composition on its subsaturated water uptake and CCN activity (Petters and Kreidenweis,

237 2007). Here, we determine κ similar to the approach of Moore et al. (2011), Jurányi et al.

238 (2011), Lathem et al. (2013), Kalkavouras et al. (2019), Kacarab et al. (2020) and others, by

239 combining the CCN measurements with the SMPS aerosol size distribution data as follows.

240 For each SMPS scan, the particle size distribution is integrated backward starting from the bin

241 with the largest-size particles – which corresponds to CCN with the lowest critical

242 supersaturation, S_{cr}. We then successively add bins with smaller and smaller diameters, until

243 the aerosol number matches the CCN concentration observed for the same time period as the

244 SMPS scan. The particles in the smallest size bin, which we call *critical dry diameter*, D_{cr},

245 correspond to CCN with highest critical supersaturation possible – being the instrument

246 supersaturation, SS. From D_{cr} and SS we determine κ from Köhler theory (Petters and

247 Kreidenweis, 2007), assuming the particle chemical composition is internally mixed:

$$\kappa = \frac{4A^3}{27D_{cr}^3 SS^2} \tag{1}$$

248 where $A = \frac{4M_w\sigma_w}{RT\rho_w}$ is the Kelvin parameter, while M_w (kg mol^{-1}), σ_w (J m^{-2}) and ρ_w (kg m^{-3}) are,

249 respectively, the molar mass, surface tension and density of water, R=8.3145 J mol^{-1} K^{-1} is the

250 universal gas constant and T (K) is the ambient temperature. The κ determined above represents

251 the composition of particles with diameter D_{cr} (large particles can have a different κ but still

252 activate given that their critical supersaturation is lower than the prevailing SS in the CCN

253   chamber). This means that over the course of an hour, over which a full SS cycle is completed,

254   κ is determined for a range of D_{cr}, which in our case were in the range of 50-200 nm (Section

255   3.1). This size-resolved κ information provides insights on the possible origin and chemical

256   components of the aerosol, which is important given that there is no other measurement

257   available to constrain chemical composition during RACLETS. From κ, we infer an equivalent

258   organic mass fraction, ε_{org}, assuming that the aerosol is composed of an organic-inorganic

259   mixture:

$$\varepsilon_{org} = \frac{(\kappa - \kappa_i)}{(\kappa_o - \kappa_i)} \tag{2}$$

260   where $\kappa_i = 0.6$ and $\kappa_o = 0.1$ are characteristic hygroscopicity values for the inorganic fraction

261   of aerosol (represented by ammonium sulphate), and aged organics, respectively (Petters and

262   Kreidenweis, 2007; Wang et al., 2008; Dusek et al., 2010). Note that these values for a

263   continental aerosol are supported by observations and analyses (e.g., Andreae and Rosenfeld,

264   2008; Rose et al., 2008; Pringle et al., 2010).

265

266   2.3 Cloud droplet number and cloud maximum supersaturation

267   Here we apply adiabatic cloud parcel theory to the observational datasets to determine the

268   maximum in-cloud supersaturation (S_{max}) and cloud droplet number (N_d) that would form over

269   both measurement sites throughout the observation period. Droplet calculations are carried out

270   with the physically based aerosol activation parameterization of Nenes and Seinfeld (2003),

271   with extensions introduced by Fountoukis and Nenes (2005), Barahona et al. (2010), and

272   Morales and Nenes (2014). Each N_d calculation requires knowledge of the observed pressure,

273   temperature, vertical winds, aerosol size distribution and hygroscopicity. For the WFJ site, all

274   data are available as described in the sections above. For the WOP site, CCN (hence

275   hygroscopicity) data are not available, so we carry out N_d calculations at two κ values, 0.1 and

276   0.25, which is the upper and the lower limit determined from the WFJ analysis (Section 3.1).

277   The ability to reproduce observed cloud droplet number concentrations ("Method evaluation",

278   Section 3.2.1) further supports the selection of these values.

279   Vertical velocity measurements are obtained from the wind lidar data extracted for the

280   altitude of interest, being 200 m and 1100 m AGL for WOP and WFJ, respectively. The

281   measured updraft velocities are then fitted to a half-Gaussian probability density function

282   (PDF) with zero mean and standard deviation σ_w. PDFs are obtained for hourly segments, while

283   an example of this calculation method is provided in the supplementary material (supplement

284   Fig. S2). Employing the "characteristic velocity" approach of Morales and Nenes (2010), the

285   PDF-averaged values of N_d and S_{max} are calculated by applying the parameterization using a

286   single characteristic velocity, $w^*=0.79\sigma_w$. This approach has been shown to successfully predict

287   cloud-scale values of N_d in field studies for cumulus and stratocumulus clouds (e.g., Conant et

288   al., 2004; Meskhidze et al., 2005; Fountoukis et al., 2007; Morales et al., 2014; Kacarab et al.,

289   2020). The droplet closure carried out in this study is also used to support the validity of this

290   approach for Alpine MPCs. The accuracy of the wind lidar products is affected by precipitation,

291   as the measured updraft velocities might be masked by the terminal fall velocity of the

292   hydrometeors. We therefore exclude precipitating periods from our analysis – using

293   disdrometer measurements to constrain periods of precipitation. Aiming to examine how N_d

294   responds to different vertical velocity-aerosol situations, as a sensitivity test, potential N_d for

295   both sites are calculated at values of σ_w between 0.1 and 1.0 ms^{-1} that cover the observed range

296   (Section 3.2.4). Note that we use the term "potential" droplet number throughout this study, as

297   its calculation is performed regardless of the actual existence of clouds over the measurement

298   sites.

299

3.   Results & Discussion

301   3.1 Particle number, CCN concentration and κ at WOP and WFJ

302   The total aerosol number concentration (N_{aer}) timeseries (integrated aerosol size distribution)

303   together with horizontal wind speed and direction measurements are depicted for both sites in

304   Figure 1. The N_{aer} data points of WFJ are colored by κ (Section 2.2), while orange dots are

305   used as a trace for WOP timeseries, as κ was not determined for the site owing to a lack of

306   corresponding CCN measurements. Aiming to interpret the aerosol variations and the potential

307   differences observed between valley and high-altitude measurements, the two-week period of

308   interest is divided into two different sub-periods. During 24 and 28 of February, a high-pressure

309   system was dominant over Europe with clear skies and elevated temperatures. During this first

310   sub-period, the N_{aer} varies considerably, and tends to follow a diurnal cycle that anticorrelates

311   between the two sites (Fig. 1a). The concentrations at WOP are most of the times elevated with

312   respect to WFJ, which is expected as the N_{aer} in the valley is higher – being influenced by local

313   sources, which during this time of the year include emissions from biomass burning (BB) (Lanz

314   et al., 2010). N_{aer} at WOP peaks in the evening, reaching up to $\sim 10^4$ cm^{-3} presumably because

315   of BB emissions in the valley which seem to stop around midnight (Fig. 1a). Up to 2 orders of

316   magnitude lower N_{aer} is measured at the same time at the WFJ site. In the afternoon, aerosol
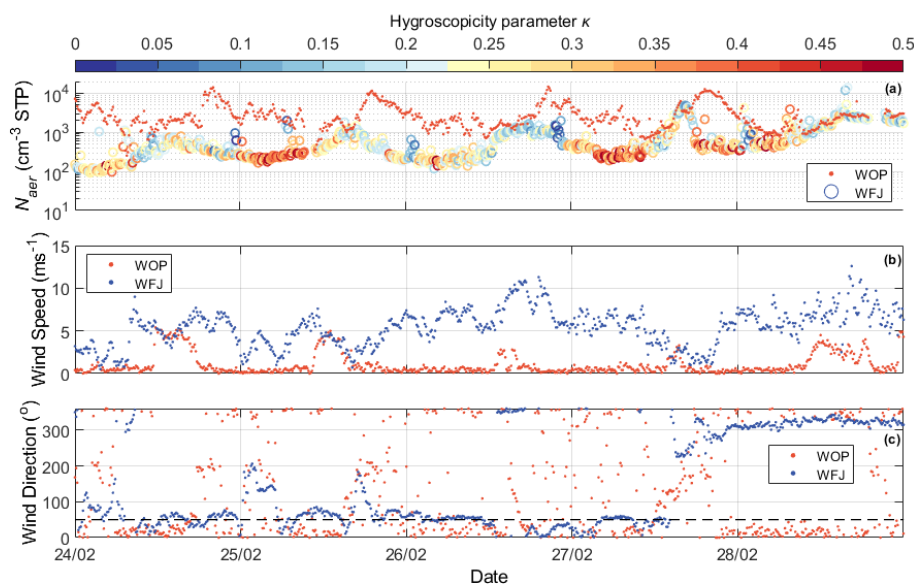
317   numbers at WFJ approach those observed at WOP, indicating that the two sites are possibly

318   experiencing similar air masses. The κ for WFJ seems to follow a clear temporal pattern as

319   well, ranging between ∽0.1-0.4 with a minimum in the afternoon, when the two sites

320   experience the same air masses. Low N_{aer} values are accompanied by higher κ, while at higher

321   N_{aer} conditions less hygroscopic aerosols are recorded (Fig. 1a).

322   The above diurnal cycles and their relationships can be understood in terms of boundary

323   layer dynamics typically occurring in mountain valley systems (Chow et al., 2013). During

324   daytime, under clear sky conditions, the slopes and the valley itself are warmed by solar

325   radiation, causing rising of the BL, and additionally the production of buoyant air masses that

326   rise up the slope toward the summit (through "up-slope" and "up-valley" winds) (Okamoto and

327   Tanimoto, 2016). This hypothesis can be further supported by the fair weather recorded by the

328   weather station at WFJ until 28 February. The buoyant upslope flow could then transport

329   polluted air masses originating from the BL of the valley up to the WFJ site, elevating the

330   concentrations of less hygroscopic aerosols observed in the afternoon. The situation reverses

331   during nighttime, when cold air descends from the slopes (down-slope winds) and flows out of

332   the valley (down-valley winds) due to the radiative cooling of the surface. The less polluted air

333   observed during the early hours of the day before sunrise indicates that the WFJ station

334   remained in the free troposphere (FT), with lower N_{aer} and more aged air (i.e. larger κ) with a

335   more prominent accumulation mode (Seinfeld and Pandis, 2006).

336   Another consideration is that the upslope flow that "connects" the valley and the

337   mountain-top site may not only be driven by thermal convection but also from mechanically-

338   forced lifting. The latter mechanism is caused by the deflection of strong winds by a steep

339   mountain slope and it can be of great importance depending mainly on the height of the

340   mountain and the mean speed of the wind (Kleissl et al., 2007). The local wind effects can be

341   further interpreted looking at the MeteoSwiss timeseries of wind speed and direction for both

342   stations (Fig. 1b, c). Wind measurements at WFJ station recorded a strong wind speed reaching

343   up to ∽11 ms^{-1} from easterly-northeasterly directions between 24 and 28 of February. The wind

344   direction measured at WFJ coincides with the relative location of WOP site (see black dashed

345   line in Fig. 1c). The steep orography over the Alps would transform part of this strong

346   horizontal motion into vertical motion, and transport air from WOP to WFJ, as seen in other

347   Alpine locations, like Jungfraujoch (e.g., Hoyle et al., 2016). A detailed analysis however is
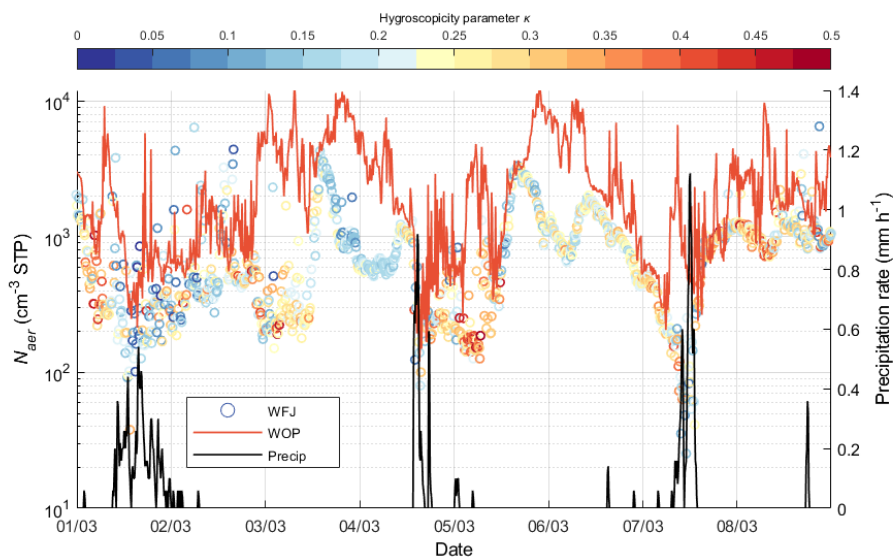
348   out of the scope of this study.

349

Figure 1. (a) N_{aer} in standard temperature and pressure conditions (cm^{-3} STP) at WOP (orange dots) and at WFJ (circles colored by κ), (b) wind speed (ms^{-1}), and (c) wind direction (in degrees) obtained from the MeteoSwiss observation stations at WFJ and Davos between 24 and 28 February 2019. The black dashed line indicates the relative direction of WOP to WFJ. Each day is referenced to 00 UTC.

Focusing on the period between 1 and 8 March, meteorological observations show the pressure and temperature dropping together with intense snow and rain events, associated with the passage of cold fronts over the region. Three precipitation events are visible in our dataset occurring on the 1st, 4th and 7th of March 2019 creating up to ∼7 mm per hour of precipitation (Fig. 2). The most intense drop in N_{aer} is seen to occur during and after the precipitation events, with the aerosol concentrations dropping to less than 200 cm^{-3} (100 cm^{-3}) at WOP (WFJ). This is not the case for the last event, where a big "spike" of N_{aer} is observed before the precipitation event in WOP timeseries, which is in contrast with the concurrent sharp decrease in N_{aer} (< 20 cm^{-3}) observed at WFJ. This could be an indication of a local source affecting the N_{aer} recorded in the valley. During dry weather conditions, we can notice again the aerosol timeseries correlating during the afternoon and anticorrelating later in the evening-early morning hours. On the 3rd of March, a steep increase in N_{aer} is seen in WFJ timeseries reaching up to ∼4000 cm^{-3}, which is followed by a period of several hours with low hygroscopicity values ($\kappa<0.2$) indicating once more the influence of freshly emitted particles arriving at WFJ from the BL of lower altitudes. Additionally, between 1 and 8 March, the diurnal cycle of particle

12

372   hygroscopicity is less pronounced. Especially on 1st and 7th of March nucleation processes or

373   precipitation scavenging removes the more hygroscopic aerosols from WFJ, thus leaving

374   behind the less effective CCN particles characterized by lower κ values (< 0.1). Also, because

375   N_{aer} drops, fresh local emissions become more important, further justifying the predominance

376   of low hygroscopicity values.

377

Figure 2. N_{aer} (cm^{-3} STP) at WOP (orange solid line) and at WFJ (circles colored by κ). The
black solid line represents the precipitation rate (mm h^{-1}) recorded from the MeteoSwiss
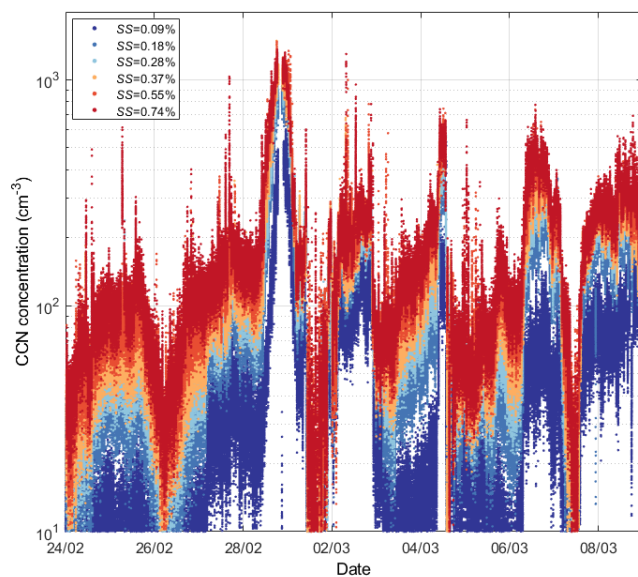observation station for each 10-min interval at WFJ between 1 and 8 of March 2019.

381

382   Figure 3 presents the CCN number concentration timeseries at WFJ for all 6

383   supersaturations measured. Throughout the two-week measurement period the recorded CCN

384   number concentrations do not seem to follow a clear temporal pattern. The absence of a diurnal

385   cycle in CCN properties measured at Jungfraujoch during winter was also pointed out in the

386   study of Jurányi et al. (2011), because the site is mainly in free tropospheric conditions during

387   most of the winter. According to Figure 3, the observed CCN concentrations tend to be low

388   ($\sim 10^2$ cm^{-3}) even at the highest SS (0.74%), which is expected given that WFJ is a remote

389   continental measurement site with CCN concentrations that are typical of FT continental air

390   (Jurányi et al., 2010, 2011; Hoyle et al., 2016; Fanourgakis et al., 2019). This is again in line

391   with the measured monthly median values of CCN (at SS=0.71%) reported by Jurányi et al.

392   (2011) being equal to 79.1 and 143.4 cm^{-3} for February and March 2009, respectively. Some

393   local CCN spikes are however recorded during the evening of 28 February and at the beginning

394   of March (e.g., on 2nd, 4th and 6th March), with the observed values of CCN reaching up to 650

395   cm^{-3} at SS=0.09% (lowest SS) and 1361 cm^{-3} at SS=0.74% (highest *SS*). Considering that WFJ

396   is a site frequently located in the FT, sudden fluctuations in the CCN concentrations could be

397   related to the vertical transport of freshly emitted particles (e.g., wood burning or vehicle

398   emissions) from the valley floor in Davos. It is also worthy to note that some aerosol spikes

399   observed on the 3rd (∽ 3350 cm^{-3}) and the 5th of March (∽ 2100 cm^{-3}) in the WFJ timeseries

400   (Fig. 1a) are not accompanied by a corresponding peak in the CCN timeseries. This indicates

401   the presence of small aerosol particles, which activate above 0.74% supersaturation (i.e.

402   particles with a diameter smaller than approx. 25 nm). This event could also be associated with

403   new particle formation (NFP) events. A previous study by Herrmann et al. (2015) reported the

404   aerosol number size distribution at the Jungfraujoch over a 6-year period indicating that NPF

405   was observed during 14.5% of the time without a seasonal preference. Tröstl et al. (2016) also

406   showed that NPF significantly adds to the total aerosol concentration at Jungfraujoch and is

407   favored only under perturbed FT conditions (i.e. BL injections). Finally, during the three

408   precipitation events (on 1st, 4th and 7th March) we can identify again that the wet removal of

409   the more hygroscopic aerosol (Fig. 2) suppresses the presence of cloud-activating particles, at

410   times depleting the atmosphere almost completely from CCN (Fig. 3). This is clearly shown

411   on the 1st and the 7th of March, when the CCN number measured at 0.74% supersaturation

412   drops below 10 cm^{-3}, which is extremely low for BL concentrations.

413   The aerosol hygroscopicity parameter derived from all CCN data collected between 24

414   of February and 8 of March is presented in Figure 4a. The red solid line represents the hourly

415   averaged hygroscopicity values over one complete instrument supersaturation cycle. The

416   hygroscopic properties of the particles at WFJ vary as a function of supersaturation, exhibiting

417   on average lower values (∽0.1) at high *SS* and higher values (∽0.3) at the lower *SS*. Since the

418   supersaturation inversely depends on particle size, Figure 4a indicates that the hygroscopicity

419   of the particles drops by almost 60% as the particles are getting smaller (i.e. as the

420   supersaturation increases). Table 2 summarizes the mean values of κ and D_{cr} and their standard

421   deviations, as calculated for each measured *SS*. The anticorrelation seen between the instrument

422   *SS* and D_{cr} is reasonable, if we consider that the latter represents the minimum activation

423   diameter in a population of particles, and therefore only the particles with a $D_{cr} > 193.54$ nm

424   are able to activate into cloud droplets at low *SS* values (0.09%). The hourly averaged

425   hygroscopicity at each *SS* slot falls within a range of ∽0.2 and ∽0.3, which is a well

426   representative value for continental aerosols (Andreae and Rosenfeld, 2008; Rose et al., 2008).

Atmospheric
Chemistry
and Physics

Discussions

Open Access

EGU

Figure 3. Timeseries of CCN number concentrations (cm^{-3}) at WFJ for different levels of supersaturation (*SS*) with respect to water between 24 February and 8 March 2019.
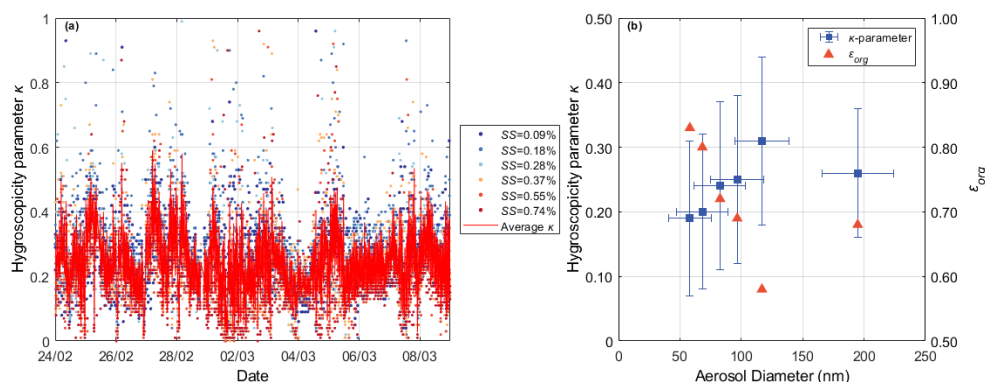
Table 2. Average κ and D_{cr} values at WFJ for each *SS* measured over the period of interest. Uncertainty for each value is expressed by the standard deviation.

SS (%)	κ_{mean}	$D_{cr,mean}$
0.09	0.26 ± 0.10	193.54 ± 29.58
0.18	0.31 ± 0.13	116.80 ± 22.20
0.28	0.25 ± 0.13	96.69 ± 21.62
0.37	0.24 ± 0.13	82.67 ± 20.93
0.55	0.20 ± 0.12	68.30 ± 20.95
0.74	0.19 ± 0.11	58.11 ± 17.54

15

Figure 4. (a) Timeseries of the hygroscopicity parameter κ at WFJ at different levels of instrument supersaturation (0.09–0.74%) throughout the period of interest. The solid red line indicates the hourly averaged κ timeseries over a complete SS cycle. (b) Size-resolved aerosol hygroscopicity (blue squares) and the respective ε_{org} (orange triangles) calculated for the WFJ site.

The hygroscopicity parameter along with the inferred ε_{org} (Eq. 2) is shown in Figure 4b as a function of particle size. Compared to smaller particles, the higher κ of larger particles (>100 nm) is consistent with them being more aged and with a lower fraction of organics. The smaller particles are possibly enriched in organic species, which is consistent with the notion that airmasses in the valley can contain large amounts of freshly emitted BB smoke with lower κ. Aerosol particles in the FT are considerably more aged (Seinfeld and Pandis, 2006) and exhibit higher values of κ and consequently lower values of ε_{org}. The chemical composition of sub-100 nm particulate matter was therefore presumably dominated by organic material transported from the valley, while the higher κ values characterizing the larger particles are consistent with the more aged character of free tropospheric aerosols (e.g., Jurányi et al., 2011). The higher ε_{org} inferred for the smaller particles suggests that mixing between fresh emissions in the valley and the free tropospheric aerosol might also be taking place at WFJ.

3.2 Potential cloud droplet number concentration and maximum supersaturation

3.2.1 Method evaluation

Figure 5 presents an overview of each measurement carried out by the HoloBalloon. Three cloud events are sampled during the 7th and the 8th of March, a more detailed description of which can be found in Ramelli et al. (2020b, c). The observed low-level clouds are likely produced by orographic lifting when the low-level flow is forced to ascent over the local topography from Klosters to WOP producing local updrafts and thus water supersaturated
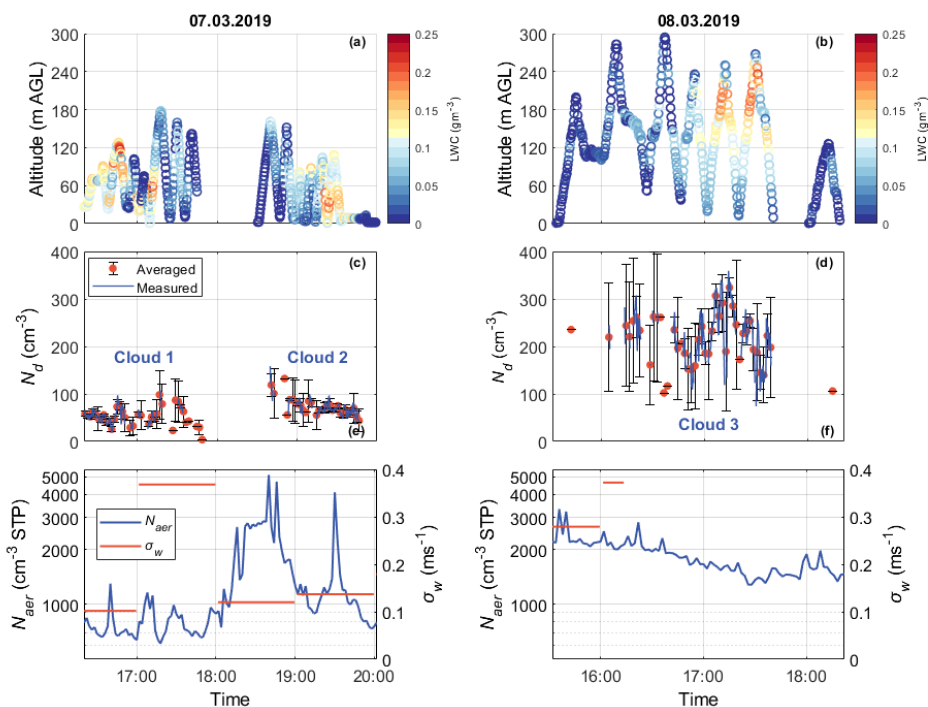
16

461   conditions. The potential droplet formation is evaluated using the updraft velocities PDF

462   calculated for each cloud period (Section 2.3). On March 8, the disdrometer recorded rainfall

463   over WOP, starting a few minutes after the development of the observed cloud system,

464   reflected in the gap of updraft velocity timeseries (Fig. 5f). In this case, to determine a relevant

465   updraft velocity from the wind lidar measurements representative of Cloud 3, we focused on a

466   15-min time period, between 16:05 and 16:20, before the precipitation occurrence. The

467   Gaussian fit to the updraft velocity gave a distribution with $\sigma_w = 0.24$ and 0.16 ms^{-1} for the first

468   two clouds present on the 7th of March, and, $\sigma_w = 0.37$ ms^{-1} for the cloud system observed on

469   the 8th of March. The w^* values used to apply the droplet parameterization are thus between

470   0.1-0.4 ms^{-1} (Section 2.3).

471   The cloud LWC measurements from the holographic imager display significant

472   temporal variability that is also related to variations in the altitude of the tethered balloon

473   system, as it tends to follow an adiabatic profile (Fig. 5a, b). Deviations from the adiabatic

474   LWC profile are likely caused by entrainment of dry air within the low-level clouds.

475   Throughout the two-day dataset presented in Figure 5, the HoloBalloon system samples at

476   altitudes lower than 300 m AGL, providing observations that are representative of BL

477   conditions. The observed N_d timeseries collected at WOP are illustrated in Figures 5c and d.

478   The measurements corresponding to LWC < 0.05 gm^{-3} are filtered out from the analysis,

479   assuming that they do not effectively capture in-cloud conditions. A similar criterion for LWC

480   was also applied in Lloyd et al. (2015) to determine the periods when clouds were present over

481   the Alpine station of Jungfraujoch. Since the measured cloud properties have finer resolution

482   (10-20 secs) than the predicted ones, the observed dataset is averaged every 2 minutes. On

483   March 7, the balloon-borne measurements were taken in a post-frontal air mass (i.e. passage of

484   a cold front in the morning) and indicated the formation of two low-level liquid layers (Fig. 5c)

485   over WOP, which is attributed to low-level flow blocking (Ramelli et al., 2020b). During the

486   first cloud event, an N_d of up to ⁓100 cm^{-3} was recorded, while slightly increased N_d in the

487   range of ⁓50-120 cm^{-3} is visible during the second cloud event. On March 8, a small-scale

488   disturbance passed the measurement location Davos, which brought precipitation (Ramelli et

489   al., 2020c). During the passage of the cloud system, the in-situ measurements collected at WOP

490   revealed the presence of a persistent low-level feeder cloud confined to the lowest 300 m of

491   the cloud. The mixed-phase low-level cloud that is shown in Figure 5d, turned into an ice-

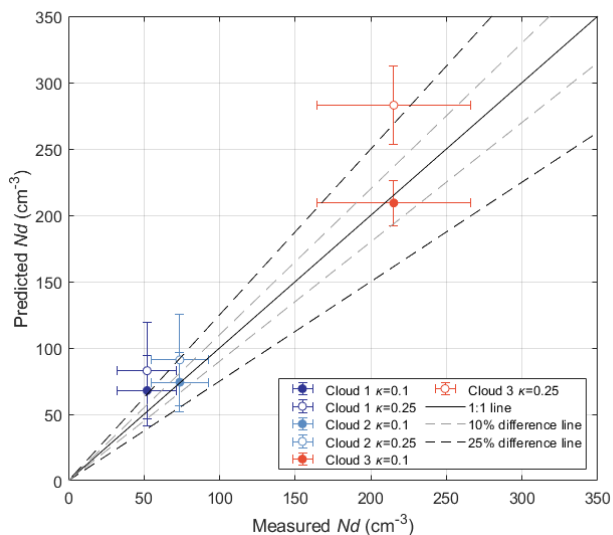492   dominated low-level cloud after 18 UTC (not shown). Throughout this event, N_d seems to range

493   between ∽100-350 cm^{-3} (Fig. 5d), while the observed ICNC was in the range of ∽1-4 L^{-1} (see

494   Fig. 6b in Ramelli et al., 2020c).

495

496

Figure 5. Timeseries of the 7th (left panels) and the 8th (right panels) of March, showing the
vertical profiles of the LWC (gm^{-3}) in (a) and (b), the filtered (blue lines) and the 2-minute
average (orange dots) N_d (cm^{-3}) measured at WOP with the HoloBalloon platform in (c) and
(d), and the corresponding SMPS aerosol concentrations (cm^{-3} STP) (blue line) and the hourly
wind-lidar derived σ_w values (ms^{-1}) (orange stars) in (e) and (f). Error bars represent the
standard deviation of N_d during the averaging period.

503

504   According to Figures 5e and f, low N_{aer} (<10^3 cm^{-3}) and intermediate σ_w values are

505   representative of the period throughout which the first cloud formed, while up to 4 times higher

506   N_{aer} is observed during the following two cloud events, with relatively low σ_w values

507   characterizing the second cloud compared to the third one. These contrasted aerosol and

508   vertical velocity regimes, in which the observed clouds are formed, offer a great opportunity

509   to test how the proposed methodology performs under a wide range of aerosol and velocity

510   conditions. Indeed, the mean cloud droplet diameters exhibit a wide range of values, which for

511   WOP range between 10 μm and 17 μm on March 7, and 8 μm to 12 μm on March 8 (not shown).

Figure 6. Comparison between average predicted N_d (cm^{-3}) with the droplet activation parameterization and N_d (cm^{-3}) observed during the three cloud events on the 7th (blue and cyan) and the 8th of March (orange) 2019. For all three cloud events droplet closure is performed assuming a κ parameter of 0.1 (filled circle) and 0.25 (empty circle). The error bars represent the standard deviation of N_d during each cloud event.

The N_d closure performed for the three cloud events observed over WOP during the last two days of the period of interest is presented in Figure 6. The parameterization predictions agree to within 25% with the in-situ cloud droplet number concentrations. A similar degree of closure is frequently obtained for other in-situ studies (e.g., Meskhidze et al., 2005; Fountoukis et al., 2007; Morales et al., 2011; Kacarab et al., 2020), which however faced on liquid-phase clouds. Here we show that the methodology can also work for mixed-phase clouds (i.e. Cloud 3 in Fig. 6). Furthermore, the parameterization predictions indicate that the best fit is achieved using a κ of ~0.1. Aerosol concentrations at WOP are likely dominated by lower κ values, indicating that the particles are getting richer in organic material, compared to WFJ, which supports the aerosol analysis carried out in Section 3.1. These results are robust, indicating that for non-precipitating BL clouds the proposed calculation method captures cloud droplet formation at WOP and WFJ.

3.2.2 Droplet formation at WOP and WFJ

According to the methodology proposed in Section 2.3, using the measured aerosol number size distribution, the estimated chemical composition and the observed updraft velocity range,

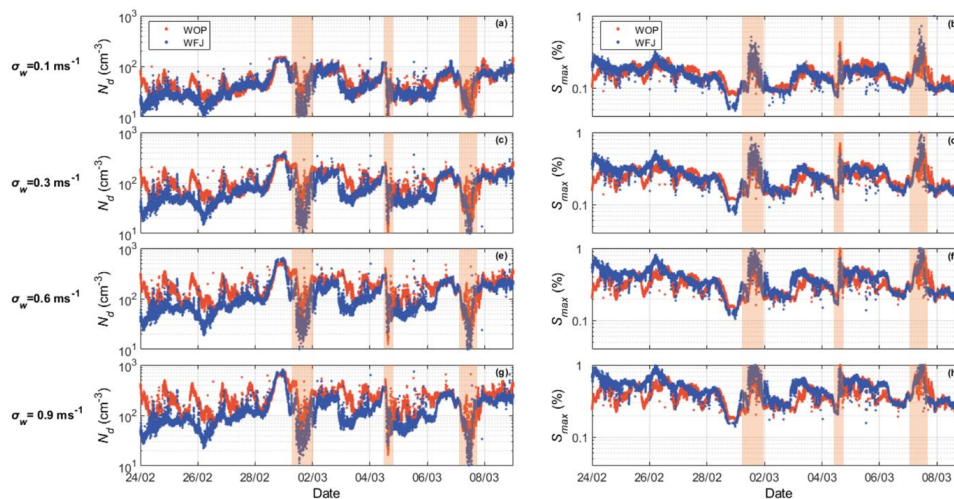535   we determine N_d and S_{max} that would form over both measurement sites. We assume a κ of 0.25

536   to calculate the potential droplets for WFJ according to our CCN-derived hygroscopicity values

537   (Table 2) and given that S_{max} usually ranges between ⌣0.1-0.3%. In estimating the potential

538   droplets for WOP, we use a κ of 0.1 given that aerosol is likely strongly enriched in organics;

539   the good degree of closure that this value provides supports its selection (Section 3.2.1). Figure

540   7 depicts the potential N_d and the corresponding S_{max} timeseries calculated for WOP (orange

541   dots) and WFJ (blue dots) using cloud updraft velocities that are indicative of the σ_w range,

542   being 0.1, 0.3, 0.6 and 0.9 ms^{-1}. The same behavior is seen for all four σ_w values selected while,

543   as expected, larger values of N_d and S_{max} are achieved at higher σ_w. During the first days of the

544   period of interest, the calculated N_d at WOP (Fig. 7a, c, e, g) is up to 10 times larger than at

545   WFJ, despite the lower κ values characterizing its aerosol population. WFJ tends to have lower

546   N_d due to the lower N_{aer} recorded. It is also important to highlight the anticorrelation between

547   S_{max} and N_d values arising from the nonlinear response of droplet number and maximum cloud

548   parcel supersaturation to fluctuations in the available aerosol/CCN concentrations (Reutter et

549   al., 2009; Bougiatioti et al., 2016; Kalkavouras et al., 2019). Higher N_{aer} elevates N_d values.

550   The available condensable water is then shared among more growing droplets, depleting the

551   supersaturation. Even more interesting is the fact that until February 28 the calculated N_d

552   timeseries at WOP show a pronounced diurnal cycle, similar to the total N_{aer} timeseries (Section

553   3.1). Lower N_d values are visible during nighttime due to the limited turbulence. Droplet

554   concentrations at WFJ do not follow a diurnal pattern in contrast to the aerosol data (Fig. 1a).

555   However, the activation fraction (i.e. N_d/N_{aer}) at WFJ displays a clear diurnal variability until

556   the end of February (supplement Fig. S3).

557   Through comparison with the MeteoSwiss precipitation measurements at WFJ (Fig. 4),

558   it should be emphasized again that during the second sub-period of interest the occurrence of

559   precipitation is followed by a depression in N_d (Fig. 7a, c, e, g) and a concurrent increase in

560   S_{max} reaching up to ⌣1% (Fig. 7b, d, f, h). Especially at WFJ N_d drops almost to zero on the

561   1st, the 4th and the 7th of March, when precipitation is most intense (orange-shaded areas on

562   Fig. 7). These trends are related to the washout of hygroscopic material observed at WFJ (Fig.

563   2) leading to the extremely low CCN concentrations (⌣10 cm^{-3}) measured during these three

564   days. During the first two precipitation events, the aerosol concentrations are relatively high,

565   compared to the third event, with concentrations reaching up to ⌣300 cm^{-3} at both stations. The

566   small activation fraction (supplement Fig. S3) combined with the high S_{max} values indicates

567   once more that small particles that activate into cloud droplets only above 0.3 to 0.5% of

568   supersaturation are present at both stations. However, this behavior is not seen on March 7 for

569   WFJ.

570

Figure 7. Calculated timeseries of N_d (cm^{-3}) (left panels) and S_{max} (%) (right panels), for updraft
velocities of $\sigma_w = 0.1$ ms^{-1} in a and b, 0.3 ms^{-1} in c and d, 0.6 ms^{-1} in e and f, and 0.9 ms^{-1} in g
and h, during the period of interest at WOP (orange dots) and WFJ (blue dots). The orange-
shaded areas represent the periods when precipitation is recorded at WFJ site, followed by a
depression in droplet number.

576

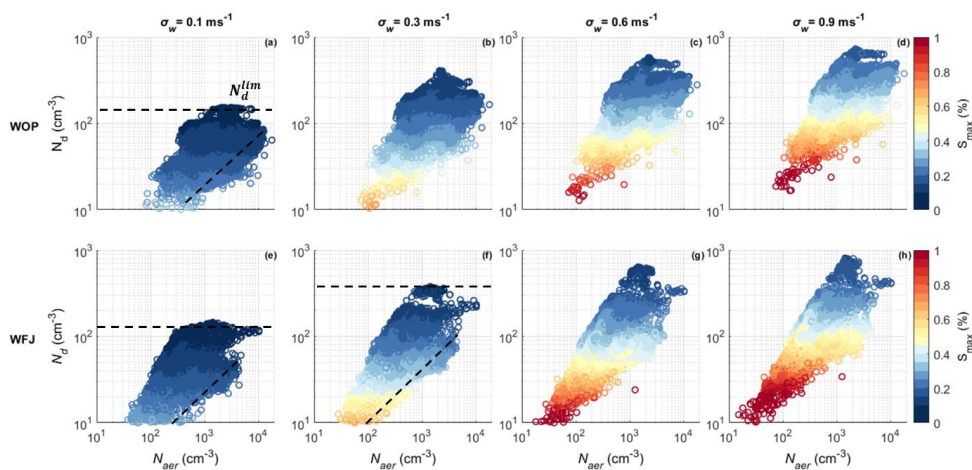577   *3.2.3 Droplet behavior under velocity-limited conditions*

578   Combining the potential N_d and the corresponding S_{max} with the aerosol size distribution data,

579   it is important to identify regimes where clouds formed are sensitive to vertical velocity

580   changes or they are sensitive to variations in aerosol concentrations. Figure 8 shows the

581   response of the calculated N_d to changes in total aerosol concentration for a representative range

582   of updraft velocities prevailing over WOP (top panels) and WFJ (bottom panels). The data are

583   colored by the respective S_{max} achieved in cloudy updrafts. For low σ_w values (Fig. 8a, d) we

584   can identify that above an aerosol concentration of $\backsim 300$ cm^{-3}, the maximum N_d at both stations

585   reaches a plateau, where its incremental change becomes insensitive to further aerosol changes.

586   At WFJ, the same behavior is seen for intermediate σ_w values and $N_{aer} \gtrsim 1000$ cm^{-3} (Fig. 8f).

587   The horizontal dashed lines plotted on Figure 8 (a), (e) and (f) illustrate this plateau, which is

588   termed limiting droplet number (N_d^{lim}), following Kacarab et al. (2020). N_d^{lim} is reached owing

589   to the extreme competition of the high aerosol concentrations for the available condensable

590   water. In this regime, the clouds are insensitive to aerosol variations and the modulation of the

591   droplet number is driven mostly by the cloud dynamics, hence the updraft velocity variability.

592   Consequently, when N_d approaches N_d^{lim} the underlying dynamics control the cloud

593   microphysics. Within the velocity-limited regime of droplet formation, we can notice that the

594   corresponding S_{max} values are low (<0.1 %), reflecting the severe water vapor limitation that

595   allows only a few particles to activate into cloud droplets. Conversely, when S_{max} in clouds

596   exceeds 0.1% droplet formation in the BL of both measurement sites is always in the aerosol-

597   limited regime, as the maximum supersaturation is high enough to activate almost all particles

598   except for the very small ones. In the aerosol-limited regime, N_d never exceeds the

599   characteristic limit, N_d^{lim}. The changeover from aerosol- to velocity-limited conditions also

600   depends on the change in slope of CCN spectra (Twomey, 1977), and that is why the transition
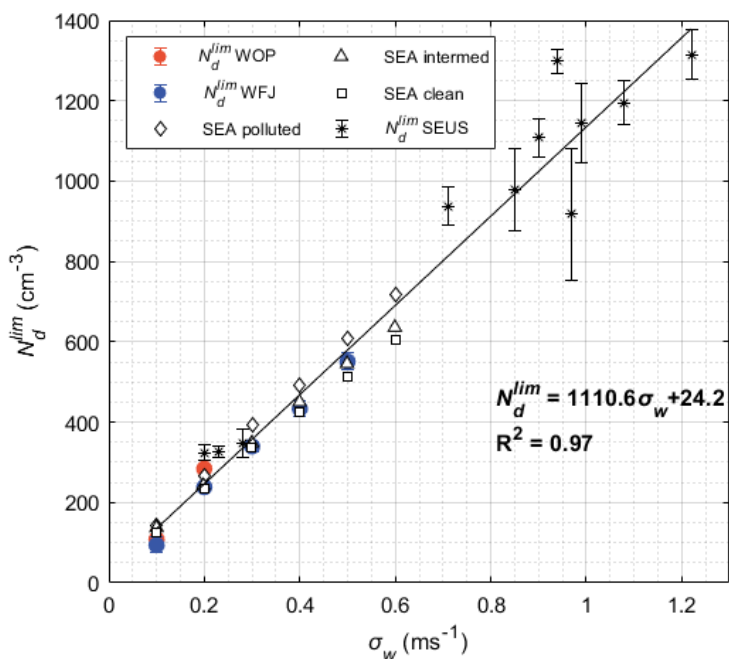
601   occurs over a region of Na (Figure 8).

602

603   **Figure 8.** N_d (cm^{-3}) vs. N_{aer} (cm^{-3}), for updraft velocities of $\sigma_w = 0.1$ ms^{-1} in a and e, 0.3 ms^{-1} in
604   b and f, 0.6 ms^{-1} in c and g and 0.9 ms^{-1} in d and h, during the period of interest at WOP (top
605   panels) and WFJ (bottom panels). Data are colored by S_{max} (%).

606

607   An alternative way of examining the N_d^{lim} response to changes in the dispersion of

608   updraft velocity is shown in Figure 9. The limiting droplet number is defined within the

609   vertical-velocity regime, assuming that this regime prevails when S_{max} drops below 0.1%. At

610   WOP, droplet formation is in the velocity-limited regime only for low σ_w values, namely 0.1

611   and 0.2 ms^{-1}, when the activated particles have more time to deplete the gas phase, and the S_{max}

612   that is reached is that required to activate only the largest particles. At WFJ the prevailing

613   dynamics create velocity-limited conditions even for more convective boundary layers when

Atmospheric
Chemistry
and Physics
Discussions

614   σ_w reaches up to 0.5 ms^{-1}. N_d^{lim} (cm^{-3}) is linearly correlated with σ_w (ms^{-1}) which can be

615   described as $N_d^{lim} = 1110.6\,\sigma_w + 24.2$ (Fig. 9). As a result, doubling σ_w from 0.1 to 0.2 ms^{-1}

616   increases N_d^{lim} by ⁓60 % for both sites, while transitioning from 0.2 to 0.4 ms^{-1} further

617   increases N_d^{lim} by ⁓45 %, and finally an additional ⁓20 % increase in N_d^{lim} occurs for WFJ

618   for the 0.4-0.5 ms^{-1} velocity range. Remarkable agreement is seen for corresponding trends

619   between N_d^{lim} and σ_w calculated for marine Stratocumulus clouds formed under extensive BB

620   aerosol plumes over the Southeast Atlantic (SEA) Ocean (Kacarab et al., 2020), along with BL

621   clouds formed in the Southeast United States (SEUS) (Bougiatioti et al., 2020). This realization

622   is important as it implies that for regions where velocity-limited conditions are expected (i.e.

623   under particularly high particle loads), $N_d{\approx}N_d^{lim}$ and the N_d^{lim}-σ_w relationship can be used to

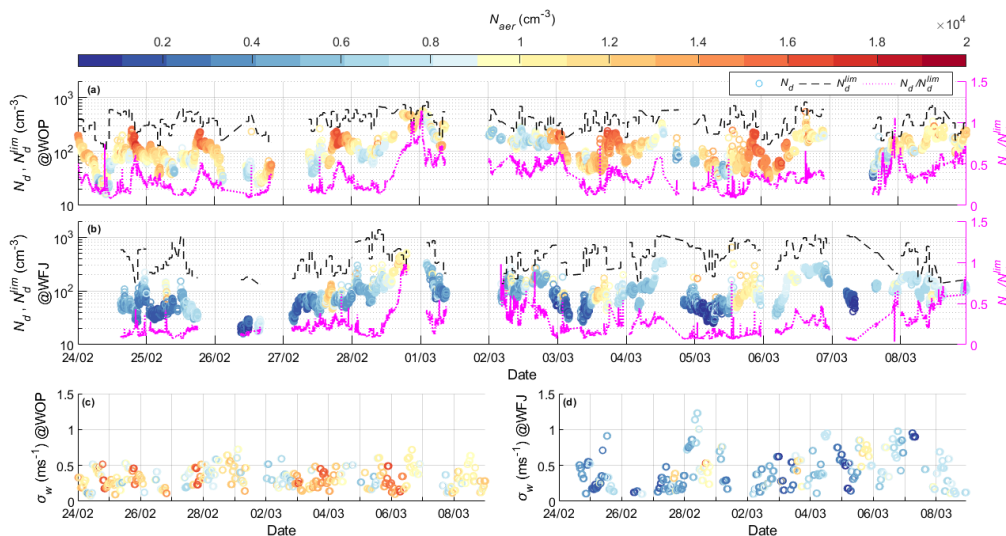624   diagnose σ_w from retrievals of droplet number for virtually any type of BL cloud.

625

Figure 9. Limiting droplet number (cm^{-3}) against the standard deviation of updraft velocity (ms^{-1}), calculated when vertical-velocity conditions are met over WOP (orange trace) and WFJ (blue trace) sites throughout the period of interest. Superimposed are the corresponding values calculated for polluted (rhombuses), intermediate (triangles) and clean (squares) conditions over the SEA Ocean and over the SEUS (asterisks).

631

23

632   *3.2.4 σ_w and observed N_d determine if droplet formation is aerosol- or velocity-limited*

633   Observations of N_d when compared against N_d^{lim} can potentially be used to deduce if droplet

634   formation is velocity- or aerosol-limited. This is important because it indicates whether aerosol

635   fluctuations are expected to result in substantial droplet number responses in clouds. The strong

636   correlation between σ_w and N_d^{lim} enables this comparison. From the σ_w timeseries together with

637   the linear N_d^{lim}-σ_w relationship (Section 3.2.3; Fig. 9) we obtain estimates of N_d^{lim} for both

638   measurement stations (black dashed line in Fig. 10a, b) and the ratio N_d/N_d^{lim} (magenta dotted

639   lines in Fig. 10a, b). The N_d timeseries calculated for WOP tend to be approximately one third

640   of N_d^{lim} for most of the observational period (colored circles in Fig. 10a, b), while for WFJ the

641   same ratio is even lower ⌣1/4. Focusing on the relatively short periods when S_{max} values drop

642   below 0.1%, we estimate that droplet formation over both measurement sites enters a velocity-

643   limited regime when the ratio N_d/N_d^{lim} exceeds a critical value of 0.5, with the most prevalent

644   value being at ⌣0.7 (supplement Fig. S4).

645

646   **Figure 10.** Timeseries of potential N_d (cm^{-3}) (circles colored by total aerosol number) along
647   with N_d^{lim} (cm^{-3}) (black dashed line) and the ratio between those two (i.e. N_d/N_d^{lim}) (magenta
648   dotted line), together with the timeseries of the calculated standard deviation of updraft
649   velocities (ms^{-1}), as estimated for WOP (a, c) and WFJ (b, d).

650

651   Throughout the period of interest velocity-limited conditions are met at WOP (WFJ)

652   with a frequency of ⌣0.5% (⌣2.5%) of the total time, reflecting again the sensitivity of droplet

653   formation to aerosol fluctuations. During nighttime however, when lower σ_w values (⌣0.1 ms$^-$

Atmospheric
Chemistry
and Physics
Discussions
Open Access
EGU

654   [1]) are recorded at WOP (Fig. 10c), we can observe some short periods characterized by

655   intermediate to high aerosol levels (> 1000 cm^{-3}) when the ratio N_d/N_d^{lim} exceeds ~0.5,

656   indicating that droplet variability is driven by updraft velocity. The standard deviation of

657   updraft velocities calculated at WFJ do not display a clear temporal pattern (Fig. 10d) but are

658   generally higher than those recorded at the valley site. This is expected considering the

659   steepness of the topography than can cause updraft velocities to be higher, especially for air-

660   masses approaching the site from the north-easterly directions. Over the high mountain-top site

661   cloud formation is in the velocity-limited regime (i.e. N_d/N_d^{lim}>0.5) under high aerosol

662   concentrations (~1500 cm^{-3}) and higher σ_w conditions (~0.8 ms^{-1}). These conditions can be

663   created when polluted air-masses from the valley site are vertically transported to WFJ.

664

4.   Summary & Conclusions

666   The current study focuses on the aerosol-CCN-cloud droplet interplay in Alpine clouds

667   sampled during the RACLETS field campaign over a two-week period of measurements

668   conducted in the valley (WOP), and at the mountain-top station (WFJ). Our main objective was

669   to investigate the drivers of droplet formation in mixed-phase clouds (MPCs) formed in the

670   region and understand in which situations droplet number is sensitive to aerosol perturbations.

671   Overall, lower N_{aer} were systematically recorded at WFJ, indicating that the site is

672   influenced by FT conditions. Deviations from this behavior are observed during fair weather

673   conditions, when injections from the BL of lower altitudes can cause up to an order of

674   magnitude elevation in the aerosol concentrations measured at WFJ. Combining the particle

675   size distribution and CCN number concentration measured at WFJ, the average hygroscopicity

676   parameter κ is about 0.25, consistent with expectations for continental aerosol. The size-

677   dependent κ reveals that accumulation mode particles are more hygroscopic than the smaller

678   ones, which we attribute to an enrichment in organic material associated with primary

679   emissions in the valley. The hygroscopicity of the particles at WFJ exhibit variations until

680   February 28, which could reflect BL injections from the valley. Precipitation events occurring

681   during the second sub-period of interest, efficiently remove particles, sometimes leaving some

682   less hygroscopic particles.

683   Wind lidar products collected at WOP constrain the PDF of updraft velocity, which

684   combined with observed size distributions and hygroscopicity can be used to calculate the N_d

685   in clouds. We show predictions to agree within 25% with the limited observations of droplet

686   number available. While this degree of closure has been achieved in past studies for liquid-

Atmospheric
Chemistry
and Physics
Discussions
Open Access
EGU

687   phase clouds, it has not been done at temperatures below freezing and with clouds containing

688   ice – as done here.

689   When σ_w is equal to 0.1 ms^{-1} droplet formation over both measurement sites is always

690   aerosol-limited if aerosol concentrations fall below ~300 cm^{-3}. For intermediate and higher σ_w

691   conditions (>0.3 ms^{-1}) the same behavior is seen, but the aerosol-limited regime is extended to

692   higher aerosol concentrations ~10^3 cm^{-3}. When droplet formation is within the velocity-limited

693   regime, it does not exceed a characteristic value, N_d^{lim}, that depends on σ_w. We found that N_d^{lim}

694   is reached when sufficient aerosol is present to decrease S_{max} below 0.1%, and corresponds to

695   when N_d/N_d^{lim} is above 0.5 for both measurement sites (with a most likely transition value at

696   0.7). Based on this understanding, we deduce that droplet formation throughout the period of

697   interest appears most of the time to be aerosol-limited. More specifically, at the valley site,

698   WOP, clouds become sensitive to updraft velocity variations only during nighttime, when the

699   BL turbulence is low. Conversely, velocity-limited conditions are encountered at WFJ, during

700   periods characterized by elevated aerosol and CCN concentration levels (>10^3 cm^{-3}) and higher

701   σ_w values (~0.8 ms^{-1}). Although variations in vertical velocity have not always been found to

702   be the strongest factor influencing the cloud microphysical characteristics, correct

703   consideration of updraft velocity fluctuations is crucial to fully understand the drivers of droplet

704   variability and the role of aerosol as a driver of N_d variability.

705   Interestingly, we find that the same linear relationship between N_d^{lim} and σ_w that

706   describes the droplet formation during RACLETS holds for warm boundary layer clouds

707   formed in the SE US (Bougiatioti et al., 2020) and in the SE Atlantic (Kacarab et al., 2019).

708   This implies that the N_d^{lim}-σ_w relationship may be universal, given the wide range of cloud

709   formation conditions it represents. If so, measurements (or remote sensing) of droplet number

710   and vertical velocity distribution alone may be used to determine if cloud droplet formation is

711   susceptible to aerosol variations or solely driven by vertical velocity – without any additional

712   aerosol information.

713   Approaching velocity-limited conditions also carries important implications for ice-

714   formation processes in MPCs – as high droplet number means that droplet size and the

715   probability of riming becomes minimum. Indeed, Lance et al. (2011) saw that the concentration

716   of large droplets exceeding 30µm diameter – critical for rime splintering or droplet shattering

717   to occur – drops considerably for polluted Arctic mixed-phase clouds with liquid content ~ 0.2

718   g m^{-3} and droplet number ~ 300-400 cm^{-3}. Assuming that these levels of droplet number reflects

719   N_d^{lim}, the corresponding σ_w is 0.3-0.35 ms^{-1} (Fig.9), which is characteristic for Arctic stratus.

Atmospheric
Chemistry
and Physics
Discussions

720   The same phenomenon can also occur in the Alpine clouds studied here, given that velocity-

721   limited conditions (N_d/N_d^{lim}>0.5) occurs especially during nighttime (Fig.10). Therefore,

722   observations of droplet number and vertical velocity distribution (i.e., N_d^{lim}) may possibly be

723   used to determine if SIP from riming and droplet shattering is impeded, and if occurring

724   frequently enough may help explain the existence of persistent MPCs.

725

726   **Data Availability:** The data used in this study can be downloaded from the EnviDat data portal

727   at   https://www.envidat.ch/group/about/raclets-field-campaign.   The   meteorological

728   measurements are provided by the Swiss Federal Office of Meteorology and Climatology

729   MeteoSwiss at https://gate.meteoswiss.ch/idaweb/login.do. The Gaussian fits used for

730   determining σ_w and the droplet parameterization used for the calculations in the study are

731   available from athanasios.nenes@epfl.ch upon request.

732

741

747

748   **Conflicts of Interest:** The authors declare no conflict of interest.

References

749 **References**

750 Andreae, M. O. and Rosenfeld, D.: Aerosol-cloud-precipitation interactions. Part 1. The nature
751 and sources of cloud-active aerosols, Earth-Science Rev., 89, 13–41,
752 doi:10.1016/j.earscirev.2008.03.001, 2008.

753 Barahona, D., West, R. E. L., Stier, P., Romakkaniemi, S., Kokkola, H. and Nenes, A.:
754 Comprehensively accounting for the effect of giant CCN in cloud activation
755 parameterizations, Atmos. Chem. Phys., 10, 2467–2473, doi:10.5194/acp-10-2467-2010,
756 2010.

757 Beck, A., Henneberger, J., Schöpfer, S., Fugal, J. and Lohmann, U.: HoloGondel: In situ cloud
758 observations on a cable car in the Swiss Alps using a holographic imager, Atmos. Meas.
759 Tech., 10, 459–476, doi:10.5194/amt-10-459-2017, 2017.

760 Bergeron, T.: On the physics of clouds and precipitation, Report, Int. Union Geod. Geophys.,
761 doi:10.1038/174957a0, 1935.

762 Borys, R. D., Lowenthal, D. H., Cohn, S. A. and Brown, W. O. J.: Mountaintop and radar
763 measurements of anthropogenic aerosol effects on snow growth and snowfall rate,
764 Geophys. Res. Lett., 30, doi:10.1029/2002gl016855, 2003.

765 Bougiatioti, A., Bezantakos, S., Stavroulas, I., Kalivitis, N., Kokkalis, P., Biskos, G.,
766 Mihalopoulos, N., Papayannis, A. and Nenes, A.: Biomass-burning impact on CCN
767 number, hygroscopicity and cloud formation during summertime in the eastern
768 Mediterranean, Atmos. Chem. Phys., 16, 7389–7409, doi:10.5194/acp-16-7389-2016,
769 2016.

770 Bougiatioti, A., Nenes, A., Lin, J., Brock, C., de Gouw, J., Liao, J., Middlebrook, A. and Welti,
771 A.: Drivers of cloud droplet number variability in the summertime Southeast United States,
772 Atmos. Chem. Phys. Discuss., doi:10.5194/acp-2020-225, accepted for publication in
773 ACP, 2020.

774 Chow, F. K., De Wekker, Stephan, F. J. and Snyder, B. J.: Mountain weather research and
775 forecasting: recent progress and current challenges., Dordrecht: Springer, 2013. Internet
776 resource.

777 Dusek, U., Frank, G. P., Curtius, J., Drewnick, F., Schneider, J., Krten, A., Rose, D., Andreae,
778 M. O., Borrmann, S. and Pöschl, U.: Enhanced organic mass fraction and decreased
779 hygroscopicity of cloud condensation nuclei (CCN) during new particle formation events,
780 Geophys. Res. Lett., 37, L03804, doi:10.1029/2009GL040930, 2010.

781 Fanourgakis, G. S., Kanakidou, M., Nenes, A., Bauer, S. E., Bergman, T., Carslaw, K. S., Grini,
782 A., Hamilton, D. S., Johnson, J. S., Karydis, V. A., Kirkevåg, A., Kodros, J. K., Lohmann,

783   U., Luo, G., Makkonen, R., Matsui, H., Neubauer, D., Pierce, J. R., Schmale, J., Stier, P.,

784   Tsigaridis, K., van Noije, T., Wang, H., Watson-Parris, D., Westervelt, D. M., Yang, Y.,

785   Yoshioka, M., Daskalakis, N., Decesari, S., Gysel Beer, M., Kalivitis, N., Liu, X.,

786   Mahowald, N. M., Myriokefalitakis, S., Schrödner, R., Sfakianaki, M., Tsimpidi, A. P.,

787   Wu, M. and Yu, F.: Evaluation of global simulations of aerosol particle number and cloud

788   condensation nuclei, and implications for cloud droplet formation, Atmos. Chem. Phys.

789   Discuss., 19, 8591–8617, doi:10.5194/acp-19-8591-2019, 2019.

790   Farrington, R. J., Connolly, P. J., Lloyd, G., Bower, K. N., Flynn, M. J., Gallagher, M. W.,

791   Field, P. R., Dearden, C. and Choularton, T. W.: Comparing model and measured ice

792   crystal concentrations in orographic clouds during the INUPIAQ campaign, Atmos. Chem.

793   Phys., 16, 4945–4966, doi:10.5194/acp-16-4945-2016, 2016.

794   Field, P. R., Lawson, R. P., Brown, P. R. A., Lloyd, G., Westbrook, C., Moisseev, D.,

795   Miltenberger, A., Nenes, A., Blyth, A., Choularton, T., Connolly, P., Buehl, J., Crosier, J.,

796   Cui, Z., Dearden, C., DeMott, P., Flossmann, A., Heymsfield, A., Huang, Y., Kalesse, H.,

797   Kanji, Z. A., Korolev, A., Kirchgaessner, A., Lasher-Trapp, S., Leisner, T., McFarquhar,

798   G., Phillips, V., Stith, J. and Sullivan, S.: Chapter 7. Secondary Ice Production - current

799   state of the science and recommendations for the future, Meteorol. Monogr.,

800   doi:10.1175/amsmonographs-d-16-0014.1, 2017.

801   Findeisen, W.: Die kolloidmeteorologischen vorgänge bei der niederschlagsbildung, Meteorol.

802   Zeitschrift, 55, 121–133, 1938.

803   Fountoukis, C. and Nenes, A.: Continued development of a cloud droplet formation

804   parameterization for global climate models, J. Geophys. Res., 110, D1121,

805   doi:10.1029/2004JD005591, 2005.

806   Fountoukis, C., Nenes, A., Meskhidze, N., Bahreini, R., Conant, W. C., Jonsson, H., Murphy,

807   S., Sorooshian, A., Varutbangkul, V., Brechtel, F., Flagan, R. C. and Seinfeld, J. H.:

808   Aerosol-cloud drop concentration closure for clouds sampled during the International

809   Consortium for Atmospheric Research on Transport and Transformation 2004 campaign,

810   J. Geophys. Res., 112, doi:10.1029/2006JD007272, 2007.

811   Fugal, J. P., Schulz, T. J. and Shaw, R. A.: Practical methods for automated reconstruction and

812   characterization of particles in digital in-line holograms, Meas. Sci. Technol., 20,

813   doi:10.1088/0957-0233/20/7/075501, 2009.

814   Ghan, S.J., Abdul-Razzak, H., Nenes, A., Ming, Y., Liu, X., Ovchinnikov, M., Shipway, B.,

815   Meskhidze, N., Xu, J., Shi, X.: Droplet Nucleation: Physically-based Parameterization and

816   Comparative Evaluation, J. Adv. Model. Earth Syst., 3, doi:10.1029/2011MS000074,

817   2011.

818   Griesche, H. J., Seifert, P., Ansmann, A., Baars, H., Barrientos Velasco, C., Bühl, J.,
819   Engelmann, R., Radenz, M. and Zhenping, Y.: Application of the shipborne remote
820   sensing supersite OCEANET for profiling of Arctic aerosols and clouds during Polarstern
821   cruise PS106, Atmos. Meas. Tech. Discuss., (December), 1–37, doi:10.5194/amt-2019-
822   434, 2019.

823   Grubisic, V. and Billings, B. J.: Climatology of the Sierra Nevada mountain-wave events, Mon.
824   Weather Rev., 136, 757–768, doi:10.1175/2007MWR1902.1, 2008.

825   Hammer, E., Bukowiecki, N., Gysel, M., Jurányi, Z., Hoyle, C. R., Vogt, R., Baltensperger, U.
826   and Weingartner, E.: Investigation of the effective peak supersaturation for liquid-phase
827   clouds at the high-alpine site Jungfraujoch , Switzerland (3580 m a . s . l .), Atmos. Chem.
828   Phys., 14, 1123–1139, doi:10.5194/acp-14-1123- 2014, 2014.

829   Hammer, E., Bukowiecki, N., Luo, B. P., Lohmann, U., Marcolli, C., Weingartner, E.,
830   Baltensperger, U. and Hoyle, C. R.: Sensitivity estimations for cloud droplet formation in
831   the vicinity of the high-alpine research station Jungfraujoch (3580 m a . s . l .), Atmos.
832   Chem. Phys., 15, 10309–10323, doi:10.5194/acp-15-10309-2015, 2015.

833   Henneberg, O., Henneberger, J. and Lohmann, U.: Formation and development of orographic
834   mixed-phase clouds, J. Atmos. Sci., 74, 3703–3724, doi:10.1175/JAS-D-16-0348.1, 2017.

835   Henneberger, J., Fugal, J. P., Stetzer, O. and Lohmann, U.: HOLIMO II: A digital holographic
836   instrument for ground-based in situ observations of microphysical properties of mixed-
837   phase clouds, Atmos. Meas. Tech., 6, 2975–2987, doi:10.5194/amt-6-2975-2013, 2013.

838   Herrmann, E., Weingartner, E., Henne, S., Vuilleumier, L., Bukowiecki, N., Steinbacher, M.,
839   Conen, F., Collaud Coen, M., Hammer, E., Jurányi, Z., Baltensperger, U. and Gysel, M.:
840   Analysis of long-term aerosol size distribution data from Jungfraujoch with emphasis on
841   free tropospheric conditions, cloud influence, and air mass transport, J. Geophys. Res.
842   Atmos., 120, 9459–9480, doi:10.1002/2015JD023660, 2015.

843   Hoyle, C. R., Webster, C. S., Rieder, H. E., Nenes, A., Hammer, E., Herrmann, E., Gysel, M.,
844   Bukowiecki, N., Weingartner, E., Steinbacher, M. and Baltensperger, U.: Chemical and
845   physical influences on aerosol activation in liquid clouds : a study based on observations
846   from the Jungfraujoch , Switzerland, Atmos. Chem. Phys., 16, 4043–4061,
847   doi:10.5194/acp-16-4043-2016, 2016.

848   IPCC: Climate Change 2013: The Physical Science Basis. Contribution of Working Group I to
849   the Fifth Assessment Report of the Intergovernmental Panel on Climate Change, edited
850   by: Stocker, T. F., Qin, D., Plattner, G.-K., Tignor, M., Allen, S. K., Boschung, Cambridge

851   Univ. Press. Cambridge, UK New York, NY, USA, 1535 pp.,
852   doi:10.1017/CBO9781107415324, 2013.

853   Jurányi, Z., Gysel, M., Weingartner, E., Decarlo, P. F., Kammermann, L. and Baltensperger,
854   U.: Measured and modelled cloud condensation nuclei number concentration at the high
855   alpine site Jungfraujoch, Atmos. Chem. Phys., 10, 7891–7906, doi:10.5194/acp-10-7891-
856   2010, 2010.

857   Jurányi, Z., Gysel, M., Weingartner, E., Bukowiecki, N., Kammermann, L. and Baltensperger,
858   U.: A 17 month climatology of the cloud condensation nuclei number concentration at the
859   high alpine site Jungfraujoch, J. Geophys. Res., 116, D1020, doi:10.1029/2010JD015199,
860   2011.

861   Kacarab, M., Lee Thornhill, K., Dobracki, A., Howell, S. G., O'Brien, J. R., Freitag, S., Poellot,
862   M. R., Wood, R., Zuidema, P., Redemann, J. and Nenes, A.: Biomass burning aerosol as
863   a modulator of the droplet number in the southeast Atlantic region, Atmos. Chem. Phys.,
864   20, 3029–3040, doi:10.5194/acp-20-3029-2020, 2020.

865   Kalkavouras, P., Bougiatioti, A., Kalivitis, N., Stavroulas, I., Tombrou, M., Nenes, A. and
866   Mihalopoulos, N.: Regional new particle formation as modulators of cloud condensation
867   nuclei and cloud droplet number in the eastern Mediterranean, Atmos. Chem. Phys., 19,
868   6185–6203, doi:10.5194/acp-19-6185-2019, 2019.

869   Kleissl, J., Honrath, R. E., Dziobak, M. P., Tanner, D., Val Martín, M., Owen, R. C. and
870   Helmig, D.: Occurrence of upslope flows at the Pico mountaintop observatory: A case
871   study of orographic flows on a small, volcanic island, J. Geophys. Res. Atmos., 112,
872   D10S3, doi:10.1029/2006JD007565, 2007.

873   Korolev, A. and Isaac, G.: Phase transformation of mixed-phase clouds, Q. J. R. Meteorol.
874   Soc., 129, 19–38, doi:10.1256/qj.01.203, 2003.

875   Lance, S., Shupe, M. D., Feingold, G., Brock, C. A., Cozic, J., Holloway, J. S., Moore, R. H.,
876   Nenes, A., Schwarz, J. P., Spackman, J. R., Froyd, K. D., Murphy, D. M., Brioude, J.,
877   Cooper, O. R., Stohl, A. and Burkhart, J. F.: Cloud condensation nuclei as a modulator of
878   ice processes in Arctic mixed-phase clouds, Atmos. Chem. Phys., 11, 8003–8015,
879   doi:10.5194/acp-11-8003-2011, 2011.

880   Lanz, V. A., Prévôt, A. S. H., Alfarra, M. R., Weimer, S., Mohr, C., Decarlo, P. F., Gianini, M.
881   F. D., Hueglin, C., Schneider, J., Favez, O., D'Anna, B., George, C. and Baltensperger,
882   U.: Characterization of aerosol chemical composition with aerosol mass spectrometry in
883   Central Europe: An overview, Atmos. Chem. Phys., 10, 10453–10471, doi:10.5194/acp-
884   10-10453-2010, 2010.

885   Lathem, T. L., Beyersdorf, A. J., Thornhill, K. L., Winstead, E. L., Cubison, M. J., Hecobian,
886   A., Jimenez, J. L., Weber, R. J., Anderson, B. E. and Nenes, A.: Analysis of CCN activity
887   of Arctic aerosol and Canadian biomass burning during summer 2008, Atmos. Chem.
888   Phys., 13, 2735–2756, doi:10.5194/acp-13-2735-2013, 2013.

889   Lauber, A., Henneberger, J., Mignani, C., Ramelli, F., Pasquier, J., Wieder, J. and Lohmann,
890   U.: Continuous secondary ice production initiated by updrafts through the melting layer in
891   mountainous regions, 2020, submitted.

892   Lloyd, G., Choularton, T. W., Bower, K. N., Gallagher, M. W., Connolly, P. J., Flynn, M.,
893   Farrington, R., Crosier, J., Schlenczek, O., Fugal, J. and Henneberger, J.: The origins of
894   ice crystals measured in mixed-phase clouds at the high-alpine site Jungfraujoch, Atmos.
895   Chem. Phys., 15, 12953–12969, doi:10.5194/acp-15-12953-2015, 2015.

896   Lohmann, U.: A glaciation indirect aerosol effect caused by soot aerosols, Geophys. Res. Lett.,
897   29(4), doi:10.1029/2001GL014357, 2002.

898   Lohmann, U.: Anthropogenic Aerosol Influences on Mixed-Phase Clouds, Curr. Clim. Chang.
899   Reports, 3, 32–44, doi:10.1007/s40641-017-0059-9, 2017.

900   Lohmann, U. and Feichter, J.: Global indirect aerosol effects: a review, Atmos. Chem. Phys.,
901   5, 715–737, doi:10.5194/acp-5-715-2005, 2005.

902   Lohmann, U., Henneberger, J., Henneberg, O., Fugal, J. P., Bühl, J. and Kanji, Z. A.:
903   Persistence of orographic mixed-phase clouds, Geophys. Res. Lett., 43, 10512–10519,
904   doi:10.1002/2016GL071036, 2016.

905   Meskhidze, N., Nenes, A., Conant, W. C. and Seinfeld, J. H.: Evaluation of a new cloud droplet
906   activation parameterization with in situ data from CRYSTAL-FACE and CSTRIPE, J.
907   Geophys. Res., 110, D1620, doi:10.1029/2004JD005703, 2005.

908   Mignani, C., Wieder, J., Sprenger, M. A., Kanji, Z. A., Henneberger, J., Alewell, C. and Conen,
909   F.: Towards parametrising atmospheric concentrations of ice nucleating particles active at
910   moderate supercooling, Atmos. Chem. Phys. Discuss., doi:10.5194/acp-2020-524, 2020.

911   Moore, R. H., Bahreini, R., Brock, C. A., Froyd, K. D., Cozic, J., Holloway, J. S., Middlebrook,
912   A. M., Murphy, D. M. and Nenes, A.: Hygroscopicity and composition of Alaskan Arctic
913   CCN during April 2008, Atmos. Chem. Phys., 11, 11807–11825, doi:10.5194/acp-11-
914   11807-2011, in review, 2011.

915   Morales Betancourt, R. and Nenes, A.: Characteristic updrafts for computing distribution-
916   averaged cloud droplet number and stratocumulus cloud properties, J. Geophys. Res., 115,
917   D1822, doi:10.1029/2009JD013233, 2010.

918   Morales Betancourt, R. and Nenes, A.: Understanding the contributions of aerosol properties

919   and parameterization discrepancies to droplet number variability in a global climate model,
920   Atmos. Chem. Phys., 14, 4809–4826, doi:10.5194/acp-14-4809-2014, 2014.
921   Morales Betancourt, R., Nenes, A., Jonsson, H., Flagan, R. C. and Seinfeld, J. H.: Evaluation
922   of an entraining droplet activation parameterization using in situ cloud data, J. Geophys.
923   Res., 116, D1520, doi:10.1029/2010JD015324, 2011.
924   Muhlbauer, A. and Lohmann, U.: Sensitivity studies of aerosol-cloud interactions in mixed-
925   phase   orographic   precipitation,   J.   Atmos.   Sci.,   66,   2517–2538,
926   doi:10.1175/2009JAS3001.1, 2009.
927   Nenes, A. and Seinfeld, J. H.: Parameterization of cloud droplet formation in global climate
928   models, J. Geophys. Res., 108, 4415, doi:10.1029/2002jd002911, 2003.
929   Nenes., A., Ghan, S., Abdul-Razzak, H., Chuang, P.Y., Seinfeld, J.H.: Kinetic Limitations on
930   Cloud Droplet Formation and Impact on Cloud Albedo, Tellus, 53B, 133-149, 2001.
931   Okamoto, S. and Tanimoto, H.: A review of atmospheric chemistry observations at mountain
932   sites, Prog. Earth Planet. Sci., 3, 34, doi:10.1186/s40645-016-0109-2, 2016.
933   Petters, M. D. and Kreidenweis, S. M.: A single parameter representation of hygroscopic
934   growth and cloud condensation nucleus activity, Atmos. Chem. Phys., 7, 1961–1971,
935   doi:10.5194/acp-7-1961-2007, 2007.
936   Pringle, K. J., Tost, H., Pozzer, A., Pöschl, U. and Lelieveld, J.: Global distribution of the
937   effective aerosol hygroscopicity parameter for CCN activation, Atmos. Chem. Phys., 10,
938   5241–5255, doi:10.5194/acp-10-5241-2010, 2010.
939   Pruppacher, H. R. and Klett, J. D.: Microphysics of Clouds and Precipitation, Kluwer Acad.,
940   Norwell, Mass., 1997.
941   Ramelli, F., Beck, A., Henneberger, J. and Lohmann, U.: Using a holographic imager on a
942   tethered balloon system for microphysical observations of boundary layer clouds, Atmos.
943   Meas. Tech., 13, 925–939, doi:10.5194/amt-13-925-2020, 2020a.
944   Ramelli, F., Henneberger, J., David, R. O., Lauber, A., Pasquier, J. T., Wieder, J., Bühl, J.,
945   Seifert, P., Engelmann, R., Hervo, M. and Lohmann, U.: Influence of low-level blocking
946   and turbulence on the microphysics of a mixed-phase cloud in an inner-Alpine valley,
947   Atmos. Chem. Phys. Discuss., doi:10.5194/acp-2020-774, in review, 2020b.
948   Ramelli, F., Henneberger, J., David, R. O., Bühl, J., Radenz, M., Seifert, P., Wieder, J., Lauber,
949   A., Pasquier, J. T., Engelmann, R., Mignani, C., Hervo, M. and Lohmann, U.:
950   Microphysical investigation of the seeder and feeder region of an Alpine mixed-phase
951   cloud, submitted manuscript, 2020c.
952   Reutter, P., Su, H., Trentmann, J., Simmel, M., Rose, D., Gunthe, S. S., Wernli, H., Andreae,

953   M. O. and Pöschl, U.: Aerosol- and updraft-limited regimes of cloud droplet formation:
954   Influence of particle number, size and hygroscopicity on the activation of cloud
955   condensation nuclei (CCN), Atmos. Chem. Phys., 9, 7067–7080, doi:10.5194/acp-9-7067-
956   2009, 2009.

957 Roberts, G. C. and Nenes, A.: A continuous-flow streamwise thermal-gradient CCN chamber
958   for atmospheric measurements, Aerosol Sci. Technol., 39(3), 206–221,
959   doi:10.1080/027868290913988, 2005.

960 Roe, G. H.: Orographic Precipitation, Annu. Rev. Earth Planet. Sci., 33, 645–671,
961   doi:10.1146/annurev.earth.33.092203.122541, 2005.

962 Rose, D., Gunthe, S. S., Mikhailov, E., Frank, G. P., Dusek, U., Andreae, M. O. and Pöschl,
963   U.: Calibration and measurement uncertainties of a continuous-flow cloud condensation
964   nuclei counter (DMT-CCNC): CCN activation of ammonium sulfate and sodium chloride
965   aerosol particles in theory and experiment, Atmos. Chem. Phys., 8(5), 1153–1179,
966   doi:10.5194/acp-8-1153-2008, 2008.

967 Rotunno, R. and Houze, R. A.: Lessons on orographic precipitation from the Mesoscale Alpine
968   Programme, Q. J. R. Meteorol. Soc., 133, 811–830, doi:10.1002/qj.67, 2007.

969 Saleeby, S. M., Cotton, W. R., Lowenthal, D. and Messina, J.: Aerosol impacts on the
970   microphysical growth processes of orographic snowfall, J. Appl. Meteorol. Climatol., 52,
971   834–852, doi:10.1175/JAMC-D-12-0193.1, 2013.

972 Seinfeld, J. H. and Pandis, S. N.: Atmospheric Chemistry and Physics: From Air Pollution to
973   Climate Change, 2nd Edn., John Wiley, edited by: Hoboken, New York, 2006.

974 Seinfeld, J. H., Bretherton, C., Carslaw, K. S., Coe, H., DeMott, P. J., Dunlea, E. J., Feingold,
975   G., Ghan, S., Guenther, A. B., Kahn, R., Kraucunas, I., Kreidenweis, S. M., Molina, M. J.,
976   Nenes, A., Penner, J. E., Prather, K. A., Ramanathan, V., Ramaswamy, V., Rasch, P. J.,
977   Ravishankara, A. R., Rosenfeld, D., Stephens, G. and Wood, R.: Improving our
978   fundamental understanding of the role of aerosol-cloud interactions in the climate system,
979   Proc. Natl. Acad. Sci. U. S. A., 113, 5781–5790, doi:10.1073/pnas.1514043113, 2016.

980 Smith, R. B.: Progress on the theory of orographic precipitation, Spec. Pap. Geol. Soc. Am.,
981   398, 1–16, doi:10.1130/2006.2398(01), 2006.

982 Sotiropoulou, G., Vignon, E., Young, G., Morrison, H., O'Shea, S. J., Lachlan-Cope T., Berne,
983   A. and Nenes, A.: Secondary ice production in Antarctic mixed-phase clouds: an
984   underappreciated process in atmospheric models, Atmos. Chem. Phys. Discuss.,
985   doi:https://doi.org/10.5194/acp-2020-328, 2020a.

986 Sotiropoulou, G., Sullivan, S., Savre, J., Lloyd, G., Lachlan-Cope, T., Ekman, A. M. L. and

987   Nenes, A.: The impact of secondary ice production on Arctic stratocumulus, Atmos. Chem.
988   Phys., 20, 1301–1316, doi:10.5194/acp-20-1301-2020, 2020b.
989 Sullivan, S. C., Lee, D., Oreopoulos, L. and Nenesa, A.: Role of updraft velocity in temporal
990   variability of global cloud hydrometeor number, Proc. Natl. Acad. Sci. U. S. A., 113,
991   5791–5796, doi:10.1073/pnas.1514039113, 2016.
992 Sullivan, S. C., Barthlott, C., Crosier, J., Zhukov, I., Nenes, A. and Hoose, C.: The effect of
993   secondary ice production parameterization on the simulation of a cold frontal rainband,
994   Atmos. Chem. Phys., 18, 16461–16480, doi:10.5194/acp-18-16461-2018, 2018.
995 Tokay, A., Wolff, D. B. and Petersen, W. A.: Evaluation of the new version of the laser-optical
996   disdrometer, OTT parsivel, J. Atmos. Ocean. Technol., 31(6), 1276–1288,
997   doi:10.1175/JTECH-D-13-00174.1, 2014.
998 Touloupas, G., Lauber, A., Henneberger, J., Beck, A. and Lucchi, A.: A convolutional neural
999   network for classifying cloud particles recorded by imaging probes, Atmos. Meas. Tech.,
1000   13(5), 2219–2239, doi:10.5194/amt-13-2219-2020, 2020.
1001 Tröstl, J., Herrmann, E., Frege, C., Bianchi, F., Molteni, U., Bukowiecki, N., Hoyle, C. R.,
1002   Steinbacher, M., Weingartner, E., Dommen, J., Gysel, M. and Baltensperger, U.:
1003   Contribution of new particle formation to the total aerosol concentration at the high-
1004   altitude site Jungfraujoch (3580masl, Switzerland), J. Geophys. Res. Atmos., 121, 11692–
1005   11711, doi:10.1002/2015JD024637, 2016.
1006 Twomey, S.: Atmospheric aerosols, Elsevier Scientific Pub. Co., 320 pp., 1977.
1007 Vosper, S. B., Wells, H., Sinclair, J. A. and Sheridan, P. F.: A climatology of lee waves over
1008   the   UK   derived   from   model   forecasts,   Meteorol.   Appl.,   20,   466–481,
1009   doi:10.1002/met.1311, 2013.
1010 Wang, J., Lee, Y. N., Daum, P. H., Jayne, J. and Alexander, M. L.: Effects of aerosol organics
1011   on cloud condensation nucleus (CCN) concentration and first indirect aerosol effect,
1012   Atmos. Chem. Phys., 8, 6325–6339, doi:10.5194/acp-8-6325-2008, 2008.
1013 Wegener, A.: Thermodynamik der Atmosphäre, Ger. Barth,Leipzig, 331 pp., 1911.
1014 Zubler, E. M., Lohmann, U., Lüthi, D., Schär, C. and Muhlbauer, A.: Statistical analysis of
1015   aerosol effects on simulated mixed-phase clouds and precipitation in the Alps, J. Atmos.
1016   Sci., 68, 1474–1492, doi:10.1175/2011JAS3632.1, 2011.
1017